Single-Phase Synchronous Inverter Control for Fault Management using Emulation Signal Generators

Shinya Sekizaki[1], Yutaka Sasaki[1], Yoshifumi Zoka[1], Naoto Yorino[1,2],
Keisuke Higashi[1], Kohei Miyamoto[1], Toshihiro Yamada[1]
Graduate School of Advanced Science and Engineering, Hiroshima University[1]
National Institute of Technology, Kure College[2], Higashi-Hiroshima[1], Kure[2], Japan

***Abstract*—Grid-forming (GFM) inverters are promising solutions for future power systems with high penetration of renewables. The successful design of GFM inverters is crucial for achieving current limiting, enabling them to withstand disturbances such as voltage sags and phase jumps in grid voltages. However, when the parameters are not properly tuned, a cascaded voltage and current controller can compromise grid stabilization performance due to issues like controller windup, post-fault recovery failure, and harmonic instability. To address this challenge, this paper proposes a dual control scheme consisting of GFM and current control that work in parallel. The dual control scheme incorporates emulation signal generators integrated with the dual controllers. This integration allows for adjusting their internal states during standby mode to track to references, enabling a seamless transition between the running and standby modes. Numerical simulations and experiments demonstrate that the proposed controller exhibits promising performance under both normal and faulted conditions.**

***Index Terms*—grid forming inverter, single-phase synchronous inverter, current limitation, fault ride through, transient stability**

I. Introduction

Grid-forming (GFM) inverters are a promising solution addressing challenges in the future power-electronic-based power systems with reduced inertia due to the integration of renewable energy sources. GFM inverters, which behave as voltage sources in normal operation, are required to limit current during grid faults, supply active/reactive current, and fault recovery capability [1]. Many researchers have proposed various current limiting control methods for GFM inverters, which can be primarily classified into three categories: virtual impedance, current limiter, and voltage limiter [1].

The virtual impedance method is an approach that achieves current limitation by increasing the virtual output impedance of the inverter, while maintaining the voltage source behavior of GFM inverters even during current limitation [2], [3]. This method avoids the issue of windup associated with current limitation using an inner current control loop and ensures that the controller automatically returns to normal operation after fault clearance. However, the performance of current limitation depends on grid and fault conditions, as well as control parameters of virtual impedance [1], [2], making its design complex [4]. Furthermore, the performance of virtual impedance methods relies on low bandwidth voltage control loop, and temporary overcurrent may be observed [3], [5], [6] during fault occurrences [1].

The current limiter method regulates the output current to follow a saturated current reference. Various approaches exist for limiting the current reference, including instantaneous limiter, magnitude limiter, and priority-based limiter [1]. While the current limiter method achieves satisfactory current limitation due to the high bandwidth of controllers, it faces challenges in supplying fault currents and robust fault recovery capability. One example of this method involves controlling the inverter in synchronization with the grid, utilizing a backup phase-locked loop (PLL), and switched to grid-following (GFL) control mode. However, the PLL can suffer from small-signal or transient stability in weak grids [2], [6], [7]. Additionally, this method may face issues of post-fault recovery failure in returning to normal operation after fault clearance [8], often attributed to voltage controller's windup issues [6]. It is crucial for current limiters with inner current control loops to design anti-windup mechanisms [2].

The current limiter is typically embedded into the inner current control loop of cascaded vector-voltage and current control. The vector voltage control consisting of dual loops for voltage and current control offers fast current control performance but can lead to harmonic instability due to interactions between the grid and the inverter [6], [9]. Furthermore, it has been noted that the inclusion of current limiting within the GFM controller can suffer from transient instability [6], [5], [10]. Controller design must consider resynchronization with the grid as a voltage source after fault clearance. It is crucial to ensure that current limitation does not compromise the stability of GFM inverters, including small-signal and transient stability, and harmonic stability [11]. Improper parameter tuning in cascaded voltage and current controllers can negatively impact grid stabilization due to issues like controller windup, post-fault recovery problems, and harmonic instability. In recent years, single-loop voltage magnitude (SLVM) control has emerged as a promising alternative to address these limitations associated with the dual loop control [6].

Current limitation is essential for GFM inverters, but it should not impair the stability of the GFM inverter, such as small-signal and transient stability and harmonic stability [12]. To tackle the problems above, we have proposed a grid

Submitted to the 23rd Power Systems Computation Conference (PSCC 2024).

stabilization controller design methodology for GFM inverters based on time-scale separation method using singular perturbation theory [13]. This approach separates the GFM controller for a normal operation from the single-loop current controller used during fault conditions. This mitigates the impact of current limitation on grid stabilization performance and avoid transient instability. During fault occurrences, the controller transitions to current control to protect the GFM inverter from overcurrent and supply fault current. Rapid post-fault recovery is essential [1], necessitating accurate and fast fault detection and clearance identification. However, these detections are intricate [5], and delays in fault and fault clearance detection, as well as in the switching of the controller, pose challenges [4]. Such delays can induce temporary overcurrent and overvoltage during fault occurrences requiring careful consideration.

This paper proposes an emulation signal generator (ESG) designing to emulate the internal states of the GFM and current controllers. The proposed approach enables parallel operation of both controllers with seamless switching between them. The GFM and current controllers can operate in either standby or running mode. The controller in standby mode does not control the inverter, while the controller in running mode controls the inverter. By ensuring that the ESG maintains consistent internal state alignment between the standby and running controllers, the method facilitates smooth transitions during switching. The proposed method is applied to single-phase synchronous inverters (SSIs) [13], [14], [15] and its effectiveness is validated through numerical simulations and experiments. The main contributions of this paper can be summarized as follows:

1) Because the GFM and the current controllers are separated, the issues caused by the cascade control of voltage and current controllers is eliminated. The controller decouples the current limiting from GFM control and can avoid transient instability in the current limitation.
2) The smooth switching between the GFM and the current control is realized by the ESG, achieving better performance in returning to the GFM control after fault clearance.

II. Emulation signal generator

Figure 1 provides an overview of the proposed controller in state-space model. The ESG operates as follows in each control:

(i) During GFM control:

The GFM controller in the running mode computes the output voltage reference v_{inv}^{GFM} to control the inverter. The current controller with ESG is in standby mode and its output v_{inv}^{PR} is not used to control the inverter. The ESG regulates the internal state of the current controller to track v_{inv}^{PR} to v_{inv}^{GFM}.

(ii) During current control:

The current controller in running mode computes output voltage reference v_{inv}^{PR} to control the inverter. The GFM controller with ESG is in standby mode and its output v_{inv}^{GFM} is not used to control the inverter. The ESG regulates the internal state of the GFM controller to track v_{inv}^{GFM} to v_{inv}^{PR}.

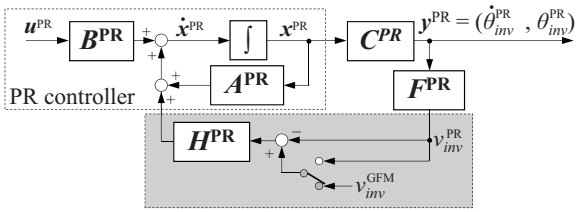

(a) GFM controller with ESG.

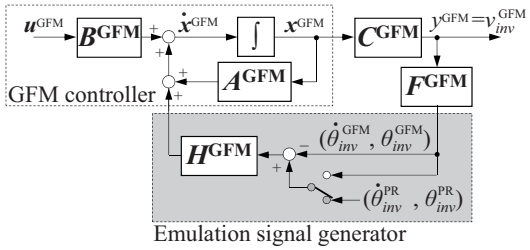

(b) PR controller with ESG.

Fig. 1: Dual controllers in state-space model.

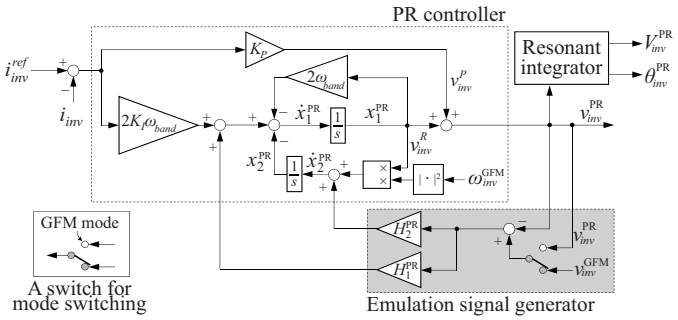

Fig. 2: A block diagram of a PR controller with ESG.

A. ESG operation during GFM control

1) Current controller in standby mode: The approximate transfer function $G_{app}^{\text{PR}}(s)$ for the proportional resonance (PR) controller used in current control is expressed by (1) [12].

$$G_{app}^{\text{PR}}(s) = K_P + K_I \frac{2\omega_{band} s}{s^2 + 2\omega_{band} s + (\omega_{inv}^{\text{GFM}})^2}, \tag{1}$$

where ω_{band} represents the bandwidth; K_P and K_I are the proportional gain and integral gain, respectively; $\omega_{inv}^{\text{GFM}}$ is the output current frequency of the inverter. Figure 2 illustrates the block diagram of the PR controller with the ESG. For the PR controller depicted in Figure 2, the internal state is denoted as $\boldsymbol{x}^{\text{PR}} = [x_1^{\text{PR}}, x_2^{\text{PR}}]^\top$, the output is $y^{\text{PR}} (= x_1^{\text{PR}})$, and the input is defined as $u^{\text{PR}} = i_{inv}^{ref} - i_{inv}$, where i_{inv}^{ref} is the current reference and i_{inv} is the output current. The state-space and output equations for the PR controller when the ESG is not active are represented by (2) and (3).

$$\dot{\boldsymbol{x}}^{\text{PR}} = \boldsymbol{A}^{\text{PR}} \boldsymbol{x}^{\text{PR}} + \boldsymbol{B}^{\text{PR}} u^{\text{PR}}, \tag{2}$$

$$y^{\text{PR}} = \boldsymbol{C}^{\text{PR}} \boldsymbol{x}^{\text{PR}} + D^{\text{PR}} u^{\text{PR}}, \tag{3}$$

where

$$\boldsymbol{A}^{\text{PR}} = \begin{bmatrix} -2\omega_{band} & -1 \\ (\omega_{inv}^{\text{GFM}})^2 & 0 \end{bmatrix}, \quad \boldsymbol{B}^{\text{PR}} = \begin{bmatrix} 2K_I\omega_{band} \\ 0 \end{bmatrix},$$
$$\boldsymbol{C}^{\text{PR}} = [1\ 0], \quad D^{\text{PR}} = K_P. \tag{4}$$

2) State-space model of ESG: Figure 2 illustrates the GFM control, and the switch at the bottom right switches to the current control. The ESG takes the deviation $(r^{\text{PR}} - y^{\overline{\text{PR}}})$ between the output voltage reference of the GFM controller, $v_{inv}^{\text{GFM}}(= r^{\text{PR}})$, and the output voltage reference of the standby PR controller, $v_{inv}^{\text{PR}}(= y^{\overline{\text{PR}}})$, as input. The ESG generates the compensation signal $\boldsymbol{H}^{\text{PR}}(r^{\text{PR}} - y^{\overline{\text{PR}}})$ to be fed into the PR controller. $\boldsymbol{H}^{\text{PR}} = [H_1^{\text{PR}}, H_2^{\text{PR}}]^\top$ represents the ESG gain vector. Using coefficients $\boldsymbol{A}^{\text{PR}}$, $\boldsymbol{B}^{\text{PR}}$, $\boldsymbol{C}^{\text{PR}}$, and D^{PR} in (4), the state-space and output equations for the PR controller with the ESG are expressed by (5) and (6).

$$\dot{\boldsymbol{x}}^{\overline{\text{PR}}} = \boldsymbol{A}^{\text{PR}}\boldsymbol{x}^{\overline{\text{PR}}} + \boldsymbol{B}^{\text{PR}}u^{\text{PR}} + \boldsymbol{H}^{\text{PR}}(r^{\text{PR}} - \hat{y}^{\text{PR}}), \tag{5}$$
$$y^{\overline{\text{PR}}} = \boldsymbol{C}^{\text{PR}}\boldsymbol{x}^{\overline{\text{PR}}} + D^{\text{PR}}u^{\text{PR}}, \tag{6}$$

where $\boldsymbol{x}^{\overline{\text{PR}}} = [x_1^{\overline{\text{PR}}}, x_2^{\overline{\text{PR}}}]^\top$, and $y^{\overline{\text{PR}}}(= x_1^{\overline{\text{PR}}})$. The notation with $\overline{\text{PR}}$ is used to distinguish $\boldsymbol{x}^{\overline{\text{PR}}}$ and $y^{\overline{\text{PR}}}$ from $\boldsymbol{x}^{\text{PR}}$ and y^{PR} in (2) and (3). Using (6) to transform (5), we have:

$$\dot{\boldsymbol{x}}^{\overline{\text{PR}}} = (\boldsymbol{A}^{\text{PR}} - \boldsymbol{H}^{\text{PR}}\boldsymbol{C}^{\text{PR}})\boldsymbol{x}^{\overline{\text{PR}}} + \boldsymbol{H}^{\text{PR}}r^{\text{PR}} + (\boldsymbol{B}^{\text{PR}} - \boldsymbol{H}^{\text{PR}}D^{\text{PR}})u^{\text{PR}}. \tag{7}$$

3) Theoretical analysis of ESG: The output equation for the resonance (R) controller extracted from the PR controller with ESG in (5) and (6) is:

$$\tilde{y}^{\text{PR}} = \boldsymbol{C}^{\text{PR}}\boldsymbol{x}^{\overline{\text{PR}}}, \quad (: y^{\overline{\text{PR}}} = \tilde{y}^{\text{PR}} + D^{\text{PR}}u^{\text{PR}}). \tag{8}$$

Using the state equation (5) and output equation (8), the transfer functions $G_u^{\text{PR}}(s)$ from input $u^{\text{PR}}(= i_{inv}^{ref} - i_{inv})$ to output $\tilde{y}^{\text{PR}}(= x_1^{\overline{\text{PR}}})$ and $G_r^{\text{PR}}(s)$ from input $v_{inv}^{\text{GFM}}(= r^{\text{PR}})$ to output $\tilde{y}^{\text{PR}}(= x_1^{\overline{\text{PR}}})$ can be derived as (9) and (10):

$$G_u^{\text{PR}}(s) = \frac{2\omega_{band}K_I s}{s^2 + (2\omega_{band} + H_1^{\text{PR}})s + ((\omega_{inv}^{\text{GFM}})^2 - H_2^{\text{PR}})}, \tag{9}$$
$$G_r^{\text{PR}}(s) = \frac{H_1^{\text{PR}}s - H_2^{\text{PR}}}{s^2 + (2\omega_{band} + H_1^{\text{PR}})s + ((\omega_{inv}^{\text{GFM}})^2 - H_2^{\text{PR}})}. \tag{10}$$

The frequency response of the transfer functions $G_u^{\text{PR}}(s)$ and $G_r^{\text{PR}}(s)$ is as follows:

$$|G_u^{\text{PR}}(j\omega)| = \frac{2\omega_{band}K_I}{\sqrt{\frac{\left((\omega_{inv}^{\text{GFM}})^2 - H_2^{\text{PR}} - \omega^2\right)^2}{\omega^2} + (2\omega_{band} + H_1^{\text{PR}})^2}}, \tag{11}$$

$$|G_r^{\text{PR}}(j\omega)| = \frac{\sqrt{(H_2^{\text{PR}})^2 + (\omega H_1^{\text{PR}})^2}}{\sqrt{((\omega_{inv}^{\text{GFM}})^2 - \omega^2 - H_2^{\text{PR}})^2 + (2\omega_{band} + H_1^{\text{PR}})^2\omega^2}}. \tag{12}$$

By increasing H_1^{PR}, the gain $|G_u^{\text{PR}}(j\omega)|$ decreases across the entire frequency range, resulting in the input u^{PR} being attenuated by $G_u^{\text{PR}}(s)$. Furthermore, when $\omega = \omega_{inv}^{\text{GFM}}$ and $\omega_{band} \ll H_1^{\text{PR}}$, the following approximations hold:

$$|G_r^{\text{PR}}(j\omega_{inv}^{\text{GFM}})| \approx \frac{\sqrt{(H_2^{\text{PR}})^2 + (\omega H_1^{\text{PR}})^2}}{\sqrt{(H_2^{\text{PR}})^2 + (\omega H_1^{\text{PR}})^2}} = 1, \tag{13}$$
$$\angle G_r^{\text{PR}}(j\omega_{inv}^{\text{GFM}}) \approx 0. \tag{14}$$

Consequently, at the frequency $\omega_{inv}^{\text{GFM}}$, the reference signal r^{PR} closely tracks $x_1^{\overline{\text{PR}}}$ through $G_r^{\text{PR}}(s)$. For frequencies $\omega \neq \omega_{inv}^{\text{GFM}}$, by increasing $H_1^{\text{PR}}(> 0)$ and decreasing $H_2^{\text{PR}}(< 0)$, the gain $|G_r^{\text{PR}}(j\omega)|$ decreases. Signals in r^{PR} containing frequencies $\omega(\neq \omega_{inv}^{\text{GFM}})$ other than those near $\omega_{inv}^{\text{GFM}}$ are attenuated.

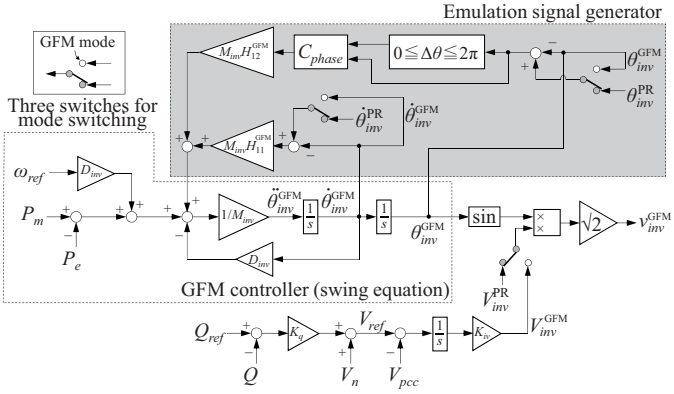

Fig. 3: A block diagram of a GFM controller with ESG.

B. ESG operation during current control

1) GFM controller in standby mode: Figure 3 illustrates the block diagram of the GFM controller with ESG in the current control. The GFM controller determines the virtual rotor angle $\theta_{inv}^{\text{GFM}}$ based on a swing equation (15) [14].

$$M_{inv}\ddot{\theta}_{inv}^{\text{GFM}} - D_{inv}\left(\omega_{ref}^{\text{GFM}} - \dot{\theta}_{inv}^{\text{GFM}}\right) = P_m - P_e, \tag{15}$$

where M_{inv} is a synthetic inertia coefficient; D_{inv} is a synthetic damping coefficient; P_m is a synthetic mechanical input; P_e is a single-phase electrical output; ω_{ref} is a frequency reference; and $\omega_{inv}^{\text{GFM}}$ is a virtual rotor frequency of the SSI.

In GFM inverter controller design, small-signal stability [7], [16] is also crucial, and SLVM control leads to better small-signal stability [6]. Thus, the GFM controller adopts the SLVM control [6], and the grid voltage is controlled using Q-V droop control (19) with an integral control (16)–(18).

$$v_{inv}^{\text{GFM}} = \sqrt{2}V_{inv}^{\text{GFM}}\sin\theta_{inv}^{\text{GFM}}, \tag{16}$$
$$V_{inv}^{\text{GFM}} = k_{iv}\int \Delta V dt, \tag{17}$$
$$\Delta V = \begin{cases} V_{ref} - V_{pcc}, & \text{if in GFM control} \\ 0, & \text{if in current control} \end{cases}, \tag{18}$$
$$V_{ref} = K_q(Q_0 - Q) + V_n, \tag{19}$$

where k_{iv} is the integral gain in the SLVM control; Q_0 is the reactive power reference; V_n is the voltage setpoint; V_{pcc} is the rms value of the grid voltage at the point of common coupling; and V_{ref} is the voltage reference obtained by Q-V

droop control. Equation (18) signifies the implementation of reactive power control in the GFM control.

Let the internal state vector of the GFM controller be denoted as $\boldsymbol{x}^{\text{GFM}} = [\dot{\theta}_{inv}^{\text{GFM}}, \theta_{inv}^{\text{GFM}}]^\top$, the output as $\boldsymbol{y}^{\text{GFM}} = [\dot{\theta}_{inv}^{\text{GFM}}, \theta_{inv}^{\text{GFM}}]^\top$, and the input as $u^{\text{GFM}} = P_m + D_{inv}\omega_{ref} - P_e$. The state-space and output equations for (15) can be expressed as (20)–(22):

$$\dot{\boldsymbol{x}}^{\text{GFM}} = \boldsymbol{A}^{\text{GFM}}\boldsymbol{x}^{\text{GFM}} + \boldsymbol{B}^{\text{GFM}}u^{\text{GFM}}, \tag{20}$$

$$\boldsymbol{y}^{\text{GFM}} = \boldsymbol{C}^{\text{GFM}}\boldsymbol{x}^{\text{GFM}}, \tag{21}$$

$$\boldsymbol{A}^{\text{GFM}} = \begin{bmatrix} -\frac{D_{inv}}{M_{inv}} & 0 \\ 1 & 0 \end{bmatrix}, \quad \boldsymbol{B}^{\text{GFM}} = \begin{bmatrix} \frac{1}{M_{inv}} \\ 0 \end{bmatrix}, \quad \boldsymbol{C}^{\text{GFM}} = \boldsymbol{I}, \tag{22}$$

where $\boldsymbol{I} \in \mathbb{R}^{2\times 2}$ represents the identity matrix.

2) State-space model of ESG: To align the frequencies $\omega_{inv}^{\text{GFM}} (= \dot{\theta}_{inv}^{\text{GFM}})$ and phase angle $\theta_{inv}^{\text{GFM}}$ of v_{inv}^{GFM} with those of the output voltage reference generated by the PR controller, v_{inv}^{PR}, which have frequency $\dot{\theta}_{inv}^{\text{PR}} (= \omega_{inv}^{\text{PR}})$ and phase angle θ_{inv}^{PR}, the internal states $\dot{\theta}_{inv}^{\text{GFM}}$ and $\theta_{inv}^{\text{GFM}}$ of the GFM controller are adjusted. In GFM control, three switches in Figure 3 are toggled.

ESG takes the deviation $(\boldsymbol{r}^{\text{GFM}} - \boldsymbol{y}^{\overline{\text{GFM}}})$ between $\boldsymbol{r}^{\text{GFM}} = [\dot{\theta}_{inv}^{\text{PR}}, \theta_{inv}^{\text{PR}}]^\top$ and $\boldsymbol{y}^{\overline{\text{GFM}}} = [\dot{\theta}_{inv}^{\text{GFM}}, \theta_{inv}^{\text{GFM}}]^\top$ as input and outputs a compensating signal $\boldsymbol{H}^{\text{GFM}}(\boldsymbol{r}^{\text{GFM}} - \boldsymbol{y}^{\overline{\text{GFM}}})$ to control the internal state $\boldsymbol{x}^{\overline{\text{GFM}}} = [\dot{\theta}_{inv}^{\text{GFM}}, \theta_{inv}^{\text{GFM}}]^\top$. To distinguish them from (20)–(22), the variables $\boldsymbol{x}^{\overline{\text{GFM}}}$ and $\boldsymbol{y}^{\overline{\text{GFM}}}$ are denoted with $\overline{\text{GFM}}$. $\boldsymbol{H}^{\text{GFM}}$ represents the ESG gain matrix. The state-space and output equations for the GFM controller with ESG are expressed in (23)–(25):

$$\dot{\boldsymbol{x}}^{\overline{\text{GFM}}} = \boldsymbol{A}^{\text{GFM}}\boldsymbol{x}^{\overline{\text{GFM}}} + \boldsymbol{B}^{\text{GFM}}u^{\text{GFM}} + \boldsymbol{H}^{\text{GFM}}(\boldsymbol{r}^{\text{GFM}} - \boldsymbol{y}^{\overline{\text{GFM}}}), \tag{23}$$

$$\boldsymbol{y}^{\overline{\text{GFM}}} = \boldsymbol{C}^{\text{GFM}}\boldsymbol{x}^{\overline{\text{GFM}}}, \tag{24}$$

$$\boldsymbol{H}^{\text{GFM}} = \begin{bmatrix} H_{11}^{\text{GFM}} & H_{12}^{\text{GFM}} \\ 0 & 0 \end{bmatrix}. \tag{25}$$

Using (24), (23) can be:

$$\dot{\boldsymbol{x}}^{\overline{\text{GFM}}} = (\boldsymbol{A}^{\text{GFM}} - \boldsymbol{H}^{\text{GFM}}\boldsymbol{C}^{\text{GFM}})\boldsymbol{x}^{\overline{\text{GFM}}} + \boldsymbol{H}^{\text{GFM}}\boldsymbol{r}^{\text{GFM}} + \boldsymbol{B}^{\text{GFM}}u^{\text{GFM}}. \tag{26}$$

Let $\Delta\theta (= \theta_{inv}^{\text{PR}} - \theta_{inv}^{\text{GFM}})$ represent the difference between θ_{inv}^{PR} and $\theta_{inv}^{\text{GFM}}$. For $0 \le \Delta\theta \le 2\pi$ rad, if $\Delta\theta$ changes between 0 rad and 2π rad in the vicinity of $\Delta\theta = 0$ rad and $\Delta\theta = 2\pi$ rad, the system (26) becomes unstable. To avoid this, a compensator C_{phase} is employed. If we denote the output of compensator C_{phase} at time t as z_t [rad] and the sampling period as Δt, then at time t, $\Delta\theta_t$ and $\Delta\theta_{t-\Delta t}$ at time $t - \Delta t$ can be used to calculate z_t as given by (27):

$$z_t = \begin{cases} \Delta\theta_t, & \text{if } |\Delta\theta_t - \Delta\theta_{t-\Delta t}| \le \pi, \\ \Delta\theta_t - 2\pi, & \text{if } \Delta\theta_t - \Delta\theta_{t-\Delta t} > \pi, \\ \Delta\theta_t + 2\pi, & \text{if } \Delta\theta_t - \Delta\theta_{t-\Delta t} < -\pi. \end{cases} \tag{27}$$

3) Theoretical analysis of ESG: Using the state equation (23) and output equation (24), the transfer function $\boldsymbol{G}_u^{\text{GFM}}(s) = [G_{u1}^{\text{GFM}}(s), G_{u2}^{\text{GFM}}(s)]^\top$ from input u^{GFM} to output $\boldsymbol{y}^{\overline{\text{GFM}}} = [\dot{\theta}_{inv}^{\text{GFM}}, \theta_{inv}^{\text{GFM}}]^\top$ can be computed by (28) and (29):

$$\boldsymbol{G}_u^{\text{GFM}}(s) = \frac{1}{D_{ur}^{\text{GFM}}(s)} \begin{bmatrix} \frac{s}{M_{inv}} \\ -\frac{1}{M_{inv}} \end{bmatrix}, \tag{28}$$

$$D_{ur}^{\text{GFM}}(s) = s^2 + \left(\frac{D_{inv}}{M_{inv}} + H_{11}^{\text{GFM}}\right)s + H_{12}^{\text{GFM}}. \tag{29}$$

$G_{u1}^{\text{GFM}}(s)$ represents the transfer function from input u^{GFM} to $\dot{\theta}_{inv}^{\text{GFM}}$, while $G_{u2}^{\text{GFM}}(s)$ represents the transfer function from input u^{GFM} to $\theta_{inv}^{\text{GFM}}$. To ensure that $\dot{\theta}_{inv}^{\text{GFM}}$ tracks $\dot{\theta}_{inv}^{\text{PR}}$ and $\theta_{inv}^{\text{GFM}}$ tracks θ_{inv}^{PR} in the current control mode, the input u^{GFM} needs to be attenuated by $\boldsymbol{G}_u^{\text{GFM}}(s)$. Calculating the frequency responses of $G_{u1}^{\text{GFM}}(s)$ and $G_{u2}^{\text{GFM}}(s)$, we obtain:

$$|G_{u1}^{\text{GFM}}(j\omega)| = \frac{\omega}{D_u^{\text{GFM}}(\omega)}, \quad |G_{u2}^{\text{GFM}}(j\omega)| = \frac{1}{D_u^{\text{GFM}}(\omega)}, \tag{30}$$

$$D_u^{\text{GFM}}(\omega) = \sqrt{M_{inv}^2(H_{12}^{\text{GFM}} - \omega^2)^2 + (D_{inv} + M_{inv}H_{11}^{\text{GFM}})^2\omega^2}. \tag{31}$$

By appropriately configuring H_{11}^{GFM} and H_{12}^{GFM}, it becomes feasible to reduce $|G_{u1}^{\text{GFM}}(j\omega)|$ and $|G_{u2}^{\text{GFM}}(j\omega)|$ across the entire frequency range, resulting in the attenuation of the input u^{GFM} through $\boldsymbol{G}_u^{\text{GFM}}(s)$.

Next, if we denote the transfer function matrix from $\boldsymbol{r}^{\text{GFM}} = [\dot{\theta}_{inv}^{\text{PR}}, \theta_{inv}^{\text{PR}}]^\top$ to $\boldsymbol{y}^{\overline{\text{GFM}}} = [\dot{\theta}_{inv}^{\text{GFM}}, \theta_{inv}^{\text{GFM}}]^\top$ as $\boldsymbol{G}_r^{\text{GFM}}(s)$, and using $D_{ur}^{\text{GFM}}(s)$ from (29), it can be expressed as:

$$\boldsymbol{G}_r^{\text{GFM}}(s) = \frac{1}{D_{ur}^{\text{GFM}}(s)} \begin{bmatrix} sH_{11}^{\text{GFM}} & sH_{12}^{\text{GFM}} \\ H_{11}^{\text{GFM}} & H_{12}^{\text{GFM}} \end{bmatrix}. \tag{32}$$

The output voltage v_{inv}^{PR} of the PR controller, controlled by the frequency $\dot{\theta}_{inv}^{\text{GFM}}$ just before transitioning to the current control mode, is determined by the integration of $\dot{\theta}_{inv}^{\text{GFM}}$ over time, given by $\theta_{inv}^{\text{PR}} = \int \dot{\theta}_{inv}^{\text{GFM}} dt$. Assuming $H_{12}^{\text{GFM}} > 0$, when the frequency $\dot{\theta}_{inv}^{\text{PR}}$ remains constant and θ_{inv}^{PR} is a ramp signal, the value of $\dot{\theta}_{inv}^{\text{GFM}}$ in a steady-state can be determined using the final value theorem:

$$\lim_{s\to 0}\left\{G_{r1}^{\text{GFM}}(s)s\frac{\dot{\theta}_{inv}^{\text{PR}}}{s} + G_{r2}^{\text{GFM}}(s)s\frac{\dot{\theta}_{inv}^{\text{PR}}}{s^2}\right\} = \dot{\theta}_{inv}^{\text{PR}}. \tag{33}$$

By using the ESG, it follows that $\dot{\theta}_{inv}^{\text{PR}} = \dot{\theta}_{inv}^{\text{GFM}}$ in a steady-state. Employing $G_{r3}(s)$ and applying the final value theorem to $\theta_{inv}^{\text{GFM}}$ (input: θ_{inv}^{PR}), the steady-state value of the output of $G_{r3}(s)$ can be determined as described in (34):

$$\lim_{s\to 0}\left\{G_{r3}(s)s\frac{\dot{\theta}_{inv}^{\text{PR}}}{s}\right\} = \frac{H_{11}^{\text{GFM}}}{H_{12}^{\text{GFM}}}\dot{\theta}_{inv}^{\text{PR}}. \tag{34}$$

The steady-state error of the ramp response of $G_{r4}(s)$, with θ_{inv}^{PR} as the input, can be calculated using (35):

$$-\frac{\frac{D_{inv}}{M_{inv}} + H_{11}^{\text{GFM}}}{H_{12}^{\text{GFM}}}\dot{\theta}_{inv}^{\text{PR}}. \tag{35}$$

The total steady-state error, considering the output of $G_{r3}(s)$ with θ_{inv}^{PR} as input and the output of $G_{r4}(s)$ with $\dot{\theta}_{inv}^{\text{PR}}$ as input, is given by:

$$\frac{H_{11}^{\text{GFM}}}{H_{12}^{\text{GFM}}}\dot{\theta}_{inv}^{\text{PR}} - \frac{\frac{D_{inv}}{M_{inv}} + H_{11}^{\text{GFM}}}{H_{12}^{\text{GFM}}}\dot{\theta}_{inv}^{\text{PR}} = -\frac{D_{inv}}{H_{12}^{\text{GFM}} M_{inv}}\dot{\theta}_{inv}^{\text{PR}}. \quad (36)$$

By increasing the gain H_{12}^{GFM}, the error approaches zero. It should be noted that when switching from current control to GFM control, the reference r^{GFM} instantaneously becomes zero (refer to Figure 3). Therefore, the ESG does not affect the GFM controller in GFM control.

The proposed controller operates by synchronizing with the grid in current control using the PR controller while performing current limiting and supplying current into the grid. Furthermore, it aligns the output v_{inv}^{GFM} of the standby GFM controller with the output v_{inv}^{PR} of the synchronized current controller. Without the need for a backup PLL, the standby GFM controller achieves synchronization with the grid without relying on a PLL, which may introduce instability in weak grids.

4) Resonant integrators: The phase angle θ_{inv}^{PR} and magnitude V_{inv}^{PR} of v_{inv}^{PR} are calculated using resonant integrators (RIs) [12]. RIs are also employed to calculate the current reference i_{inv}^{ref} used in the current control, and i_{inv}^{ref} is calculated by (37) and (38):

$$\begin{aligned}
&\dot{i}_1^{RI} = i_2^{RI}, \\
&\dot{i}_2^{RI} = \begin{cases} i_{inv} - (\omega_{inv}^{\text{GFM}})^2\ i_1^{RI} - K_r^i\ i_2^{RI}, \\ \qquad \text{(in GFM control)}, \\ -(\omega_{inv}^{\text{GFM}})^2\ i_1^{RI}, \\ \qquad \text{(in current control)}, \end{cases} \quad (37) \\
&i_{inv}^{ref} = \alpha_i K_r^i\ i_2^{RI}, \\
&\alpha_i = \begin{cases} 1.0, \quad \text{if} \quad I_{mag} \le I_{max} \quad \text{or in GFM control}, \\ \frac{I_{mag}}{I_{max}}, \quad \text{otherwise}, \end{cases} \\
&I_{mag} = \sqrt{(K_r^i\ \omega_{inv}^{\text{GFM}}\ i_1^{RI})^2 + (K_r^i\ i_2^{RI})^2}, \quad (38)
\end{aligned}$$

where K_r^i is the gain responsible for controlling the rise time of the RIs, I_{max} represents the upper limit for the output current of the inverter, and α_i is a coefficient used to limit the magnitude of the output current reference. By using (37) and (38), i_{inv}^{ref} is calculated in a manner that it equals i_{inv} during the GFM control and preserves the value of sine signal i_{inv}^{ref} from the GFM control in the current control. This enables the SSI to operate as a voltage source as much as possible until just before transitioning to the current control, while supplying fault currents into the grid in the current control.

C. Fault occurrence and clearing detection

If the absolute value of the output current, $|i_{inv}|$, exceeds the threshold value, i_{th}, the controller will detect a fault occurrence and switch to the current control. If the magnitude of voltage at the point of common coupling, v_{pcc}, exceeds the threshold value, v_{th}, the controller will also transition to the current control.

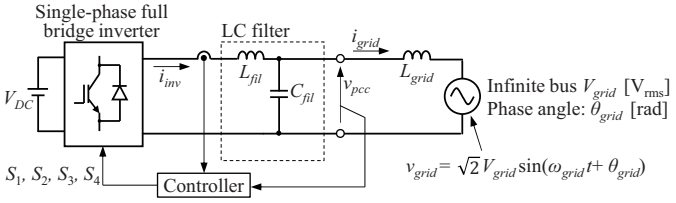

Fig. 4: Simulation model.

TABLE I: Simulation parameters.

Design parameters	Symbol	Value
Rated grid voltage (rms)	–	100 V (1.0 p.u.)
Grid frequency	ω_{grid}	$2\pi \times 60$ rad/s
Switching frequency	–	10 kHz
Filter inductance	L_{fil}	3 mH (0.113 p.u.)
Filter capacitor	C_{fil}	11 μF (0.0415 p.u.)
Grid inductance	L_{grid}	11 mH (0.0415 p.u.)
A synthetic inertia constant	M_{inv}	4
A synthetic damping coefficient	D_{inv}	200
A synthetic mechanical input	P_m	1 kW (1.0 p.u.)
Rated reactive power	Q_0	0 kvar
Set point of voltage	V_n	100 V
Reference frequency	ω_{ref}	$2\pi \times 60$ rad/s
DC voltage	V_{DC}	200 V
An SLVM gain	k_{iv}	1.0
Q-V droop gain	K_q	0.5
Threshold of current	i_{th}	20 A
Threshold of voltage	v_{th}	134.4 V (0.95 p.u.)
Upper bound of current	I_{max}	20 A

III. Numerical simulation

A. simulation conditions

A single-phase full-bridge inverter equipped with the proposed controller was connected to a voltage source representing the grid. Its rms voltage (V_{grid}) and phase angle (θ_{grid}) of the voltage source were varied. Figure 4 shows the model used for the simulation in MATLAB/Simulink, and Table I provides the relevant parameters. The inverter is connected to an infinite bus, which is depicted by the voltage source v_{grid} (ω_{grid} [rad/s]), through an LC filter consisting of L_{fil} and C_{fil}, along with a grid-side impedance characterized by inductance L_{grid}. To target a weak grid with a short circuit ratio (SCR), L_{grid} was chosen such that SCR = 2.38. For the ESG gains, the values were determined as follows: $H_1^{\text{PR}} = 10^6$, $H_2^{\text{PR}} = 10^8$, $H_{11}^{\text{GFM}} = 10^3$, $H_{12}^{\text{GFM}} = 10^6$.

(Case 1: voltage sag) The voltage V_{grid} was dropped from 1.0 p.u. to 0.1 p.u. to simulate a voltage sag, which persisted from $t = 0.00$ s to $t = 0.08833$ s (5 cycles).

(Case 2: phase jump) To simulate a phase jump, θ_{grid} was varied from 0 rad to $\pi/3$ rad (60 degrees) and was sustained from $t = 0.0$ s to $t = 0.40$ s.

(Case 3: transient stability) To evaluate the impact of the proposed controller on the transient stability of the SSI, V_{grid} was dropped from 1.0 p.u. to 0.1 p.u. and was sustained from $t = 0.00$ s to $t = 0.40$ s. After that, V_{grid} was recovered to 1.0 p.u. and the SSI switched to the GFM control.

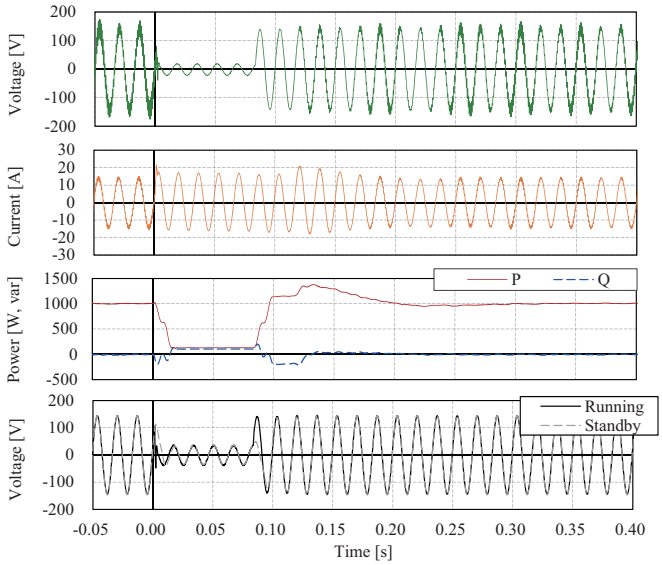

Fig. 5: (Case1) Simulation results when the grid voltage V_{grid} drops from 1.0 p.u. to 0.1 p.u.

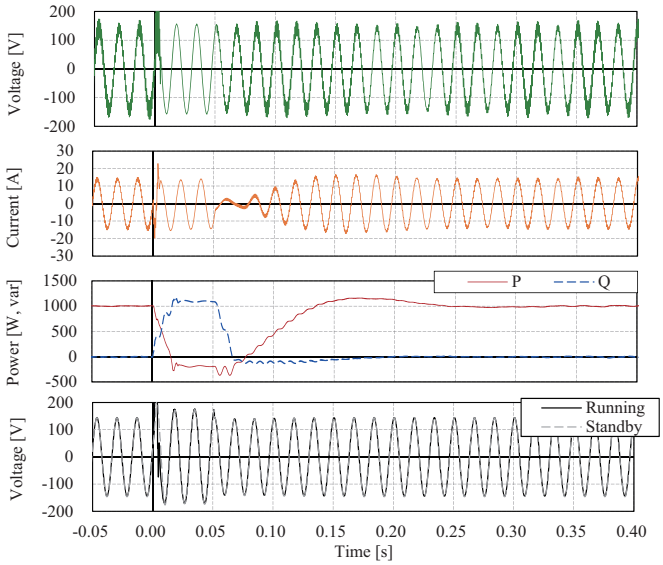

Fig. 6: (Case 2) Simulation results when the grid phase angle θ_{grid} changed from 0.0 rad to $\pi/3$ rad.

B. Simulation results

In the following three cases, even under weak grid conditions, the GFM controller remains stable under normal operating conditions.

1) Voltage sag: The simulation results for voltage sag occurrence are illustrated in Figure 5. In Figure 5, the top figure displays voltage v_{pcc} at the point of common coupling, the second one depicts current i_{inv}, and third one shows power P_e and Q. The bottom figure shows a comparison between the voltage reference of the running controller (black solid line) and the voltage reference of the standby controller (gray dashed line) (running controller: GFM controller before and after voltage sag, current controller during voltage sag).

It can be observed from Figure 5 that during voltage sag, the controller switches to the current control after detecting overcurrent, limiting the current. After the voltage sag is resolved, the controller successfully returns to the GFM control at $t = 0.11$ s without encountering overcurrent. Although there is a slight transient delay immediately following the voltage sag and its recovery, the ESG ensures that the voltage reference of both the current controller and the GFM controller align, enabling a swift return to normal operation.

2) Phase jump: Similar to Figure 5, the simulation results for the phase jump are shown in Figure 6. It can be observed that after the phase jump, the controller switches to the current control after detecting overcurrent, limiting current. After switching to the current control, the magnitude of grid voltage v_{pcc} exceeds v_{th} = 134.4 V, resulting in a return to the GFM mode around $t = 0.05$ s.

3) Transient stability: Figure 7 shows the simulation results when the grid voltage V_{grid} drops from 1.0 p.u. to 0.1 p.u. The top figure displays the voltage v_{pcc}, and the bottom one shows the phase difference δ representing the difference between the phase angle of the SSI output voltage and the phase angle θ_{grid}

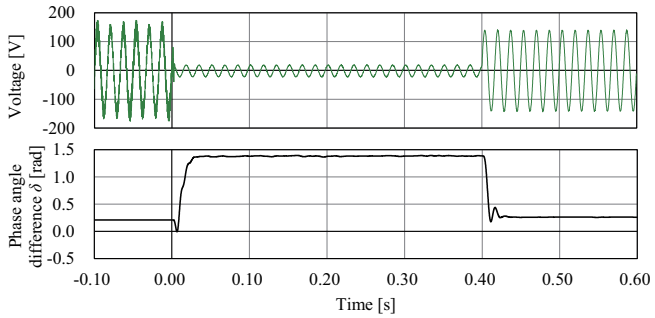

Fig. 7: (Case 3) Simulation results when the grid voltage V_{grid} drops from 1.0 p.u. to 0.1 p.u.

of the grid voltage. It can be observed from Figure 7 that even during the severe voltage sag, the proposed controller ensures transient stability. Although the inclusion of current limiting within the GFM controller can suffer from transient instability, the proposed controller separates the GFM and the current controller and avoid transient instability in the current limitation, achieving better performance in returning to the GFM control after fault clearance.

IV. Experimental Results

To verify the effectiveness of the proposed controller, the experimental tests are conducted. The proposed controller was implemented on a digital processing board controller (PE-Expert4: Myway Plus Co.), generating gate signals to drive a single-phase inverter (MINV-1R022, Myway Plus Co.). The inverter is connected through a filter (an inductance $L_{fil} = 10$ mH and a noise filter (NBH-20-432: Cosel Co. LTD.) to a grid-simulated power supply (DP series Type R: DP030RS, NF Co.). Its magnitude is set to $V_{grid} = 100$ V (rms value. 1.0 p.u.). The dc side voltage of the inverter is controlled to be $192 \leq V_{DC} \leq 196$ V by batteries (42B19R-MF). The

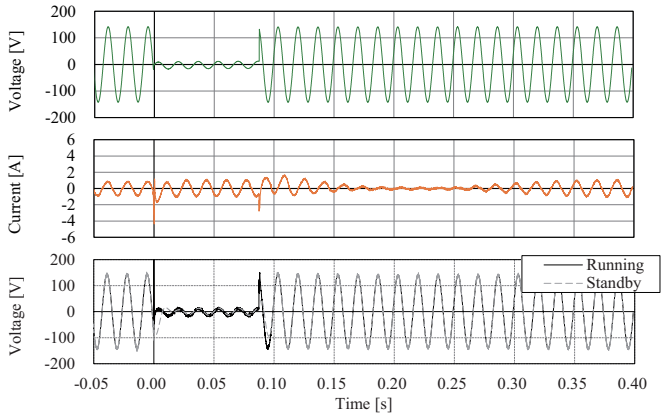

Fig. 8: Experimental results when the grid voltage V_{grid} drops from 1.0 p.u. to 0.1 p.u.

parameters M_{inv}, D_{inv}, ω_{ref} are set to the values shown in Table I. The current and voltage thresholds, i_{th} and v_{th}, respectively, are set to 3.5 A and 134.4 V. Other parameters are adjusted to suit the experimental environment. Similar to Case 1 in simulations, V_{grid} was dropped from 1.0 p.u. to 0.1 p.u., persisting from $t = 0.00$ s to $t = 0.0833$ s. The experimental result is shown in Figure 8 similar to Figures 5 and 6. It can be observed from Figure 8 that the ESG regulates the internal states of the controllers in standby mode. The proposed controller successfully limits the current during the fault condition and smoothly recovers to GFM control after fault clearance.

V. Discussion and Future Works

Tuning the parameters of a cascade controller with voltage and current control loops is a complex process. The proposed controller utilizes separate GFM and current controllers, resulting in a non-cascaded control structure under both normal and fault conditions. It operates as a voltage source during normal operation without requiring a PLL. Additionally, the controller decouples from GFM control during current limiting, thereby mitigating transient instability and enabling a smooth transition back to GFM control after fault clearance.

Utilizing three-phase active and reactive power measurements in the GFM control would enable the calculation of both the phase and magnitude for the three-phase output voltage reference. As the PR controller employed for current limiting is applicable with three-phase operation, the proposed controller can also be used for three-phase inverters. Since individual ESG implementations are required for each phase in unbalanced three-phase circuits, the application to the three-phase GFM inverters considering unbalanced conditions is one of our future works.

VI. Conclusion

This paper proposes an ESG designed to emulate the internal states of both the GFM and current controllers. The proposed controller integrated with the ESG enables the parallel operation of the dual controllers, ensuring smooth transitions between them. Through numerical simulations and experiments, it has been verified that the proposed controller operates stably as a GFM inverter in a weak grid, and can limit current during a fault condition.

Acknowledgment

This research is based on results obtained from a project, JPNP22003, commissioned by the New Energy and Industrial Technology Development Organization (NEDO).

References

[1] B. Fan, T. Liu, F. Zhao, H. Wu and X. Wang, "A review of current-limiting control of grid-forming inverters under symmetrical disturbances," *IEEE Open J. Power Electron.*, vol. 3, pp. 955–969, (2022).

[2] M. G. Taul, X. Wang, P. Davari, and F. Blaabjerg, "Current limiting control with enhanced dynamics of grid-forming converters during fault conditions," *IEEE J. Emerg. Sel. Top. Power Electron.*, vol. 8, no. 2, pp. 1062–1073, (2020).

[3] E. Rokrok, T. Qoria, A. Bruyere, B. Francois, and X. Guillaud, "Transient stability assessment and enhancement of grid-forming converters embedding current reference saturation as current limiting strategy," *IEEE Trans. Power Syst.*, vol. 37, no. 2, pp. 1519–1531, (2022).

[4] Joseba Erdocia, Andoni Urtasun, and Luis Marroyo, "Dual voltage-current control to provide grid-forming inverters with current limiting capability," *IEEE J. Emerg. Sel. Top. Power Electron.*, vol. 37, no. 4, pp. 4751–4763, (2022).

[5] T. Qoria, F. Gruson, F. Colas, X. Kestelyn, and X. Guillaud, "Current limiting algorithms and transient stability analysis of grid-forming VSCs," *Elect. Power Syst. Res.*, vol. 189, no. 106726, (2020).

[6] T. Liu, X. Wang, F. Liu, K. Xin, and Y. Liu, "A current limiting method for single-loop voltage-magnitude controlled grid-forming converters during symmetrical faults," *IEEE Trans. Power Elect.*, vol. 37, no. 4, pp. 4751–4763, (2022).

[7] C. Yang, L. Huang, H. Xin and P. Ju, "Placing grid-forming converters to enhance small signal stability of PLL-integrated power systems," *IEEE Trans. Power Syst.*, vol. 36, no. 4, pp. 3563–3573, (2021).

[8] B. Fan and X. Wang, "Fault recovery analysis of grid-forming inverters with priority-based current limiters," *IEEE Trans. Power Syst.*, vol. 38, no. 6, pp. 5102–5112, (2023).

[9] X. Wang and F. Blaabjerg, "Harmonic stability in power electronic-based power systems: concept, modeling, and analysis," *IEEE Trans. Smart Grid*, vol. 10, no. 3, pp. 2858–2870, (2019).

[10] L. Huang, H. Xin, Z. Wang, L. Zhang, K. Wu, and J. Hu, "Transient stability analysis and control design of droop-controlled voltage source converters considering current limitation," *IEEE Trans. Smart Grid*, vol. 10, no. 1, pp. 578–591, (2019).

[11] L. Huang, C. Wu, D. Zhou and F. Blaabjerg, "A power-angle-based adaptive overcurrent protection scheme for grid-forming inverter under large grid disturbances," *IEEE Trans. Ind. Electron.*, vol. 70, no. 6, pp. 5927–5936, (2023).

[12] N. Baeckeland, D. Venkatramanan, M. Kleemann and S. Dhople, "Stationary-frame grid-forming inverter control architectures for unbalanced fault-current limiting," *IEEE Trans. Energy Conv.*, vol. 37, no. 4, pp. 2813–2825, (2022).

[13] N. Yorino, S. Sekizaki, K. Adachi, Y. Sasaki, Y. Zoka, A. Bedawy, T. Shimizu, K. Amimoto, "A novel design of single-phase microgrid based on non-interference core synchronous inverters for power system stabilization," *IET Gen., Trans. & Dist.*, vol. 17, no. 12, pp. 2861–2875, (2023).

[14] S. Sekizaki, N. Yorino, Y. Sasaki, Y. Zoka, T. Shimizu, and I. Nishizaki, "Single-phase synchronous inverter with overcurrent protection using current controller with latched limit strategy," *IEEJ Trans. Elect. and Electron. Eng.*, vol. 18, no. 6 pp. 1001–1014, (2023).

[15] N. Yorino, Y. Zoka, Y. Sasaki, S. Sekizaki, M. Yokonuma, T. Himuro, F. Kuroki, T. Fujii, H. Inoue, "Development of single-phase synchronous inverter for single-phase microgrid," *Electronics*, vol. 13, no. 3, 478, (2024).

[16] U. Markovic, O. Stanojev, P. Aristidou, E. Vrettos, D. S. Callaway, and G. Hug, "Understanding small-signal stability of low-inertia systems," *IEEE Trans. Power Syst.*, vol. 36, no. 5, pp. 3997–4017, (2021).